Robust 3-D Plane Segmentation From Airborne Point Clouds Based on *Quasi-A-Contrario* Theory

Xianzhang Zhu, Xinyi Liu, Yongjun Zhang, Yi Wan, and Yansong Duan

***Abstract*—Three-dimensional (3-D) plane segmentation has been and continues to be a challenge in 3-D point cloud processing. The current methods typically focus on the planar subsets separation but ignore the requirement of the precise plane fitting. We propose a *quasi-a-contrario* theory-based plane segmentation algorithm, which is capable of dealing with point clouds of severe noise level, low density, and high complexity robustly. The main proposition is that the final plane can be composed of basic planar subsets with high planar accuracy. We cast planar subset extraction from the point set as a geometric rigidity measuring problem. The meaningfulness of the planar subset is estimated by the number of false alarms (NFA), which can be used to eliminate false-positive effectively. Experiments were conducted to analyze both the planar subset extraction and the 3-D plane segmentation. The results show that the proposed algorithms perform well in terms of accuracy and robustness compared with state-of-art methods. Experimental datasets, results, and executable program of the proposed algorithm are available at https://skyearth.org/publication/project/QTPS.**

***Index Terms*—*A-contrario*, airborne point cloud, number of false alarms (NFA), supervoxel segmentation, three-dimensional (3-D) plane segmentation.**

I. Introduction

THREE-DIMENSIONAL (3-D) point clouds acquired by airborne LiDAR system (ALS) and multiview stereo (MVS) techniques have been widely used in georegistration [1], object extraction [2], and surface reconstruction [3]. Explicit features or shapes extracted from discrete points, especially planar features, provide crucial clues for subsequent applications including building information model reconstruction [4]–[6], simultaneous localization and mapping [7], and point cloud registration [8]. Despite decades of exploration, the robustness and efficiency of the existing 3-D plane segmentation methods still cannot meet the requirements of various point clouds, which are frequently contaminated with noise, outliers, and occlusion.

Most of the existing plane segmentation methods focus on the planar points subset separation but ignore the requirement of the precise plane fitting. However, when dealing with point clouds of severe noise level, the planar parameters may be imprecise, which introduces errors for subsequent applications such as building reconstruction.

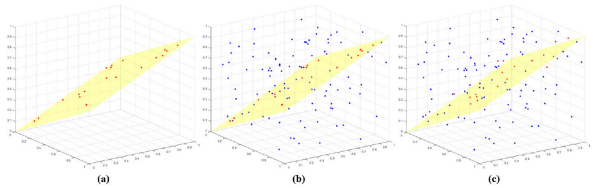

Fig. 1. Array of planar points in (a) is embedded into an array of discrete points in (b), where planar points are shown in red, discrete points are shown in blue, and the plane is shown in yellow. The planar structure is less recognizable in (b) compared with that in (a) because of the much lower proportion of planar points. If we move some of the planar points to make the planar structure less accurate as in (c), the planar structure becomes barely perceptible by human eyes. It can be concluded that the strength of a planar gestalt is affected by the number (or scale) and precision of the planar points.

The *a-contrario* theory can be employed to model the structures as gestalts perceived by human eyes based on the Helmholtz principle and the definition of ε-meaningful events, where the Helmholtz principle supplies a probabilistic view about why some gestalts can immediately draw human's visual attention [9]. Fig. 1 illustrates an example to explain why some planar gestalt is strong enough to be visually perceived. In this article, we offer a probabilistic definition for the planar-rigidity of a set of points and propose a *quasi-a-contrario* theory-based plane segmentation (QTPS) algorithm to segment accurate planes from dense ALS point cloud, sparse ALS point cloud, and MVS point cloud. The proposed algorithm first segments the point cloud into planar structures by multiscale supervoxel segmentation [10] and saliency features [11]. As the crucial technique of QTPS, *a-contrario* theory is employed to extract the planar subset from the planar structures and further evaluate the meaningfulness. Since a nonrigorous white noise background is adopted in the proposed algorithm, the name *quasi-a-contrario* being coined for the difference. The ultimate planes are generated by a region growing process. The main contributions of this article are as follows:

1) The proposed algorithm casts planar subset extraction from the point set as a geometric rigidity measuring problem, which does not require presetting hard threshold.
2) A criterion is established to evaluate the meaningfulness of the planar subset.
3) The proposed algorithm significantly reduces the influence of noise points and obtains precise planar parameters.

Manuscript received March 4, 2021; revised May 24, 2021 and June 6, 2021; accepted June 27, 2021. Date of publication June 30, 2021; date of current version July 28, 2021. This work was supported by the National Natural Science Foundation of China under Grant 41871368. *(Corresponding author: Xinyi Liu, Yongjun Zhang)*

The authors are with the School of Remote Sensing and Information Engineering, Wuhan University, Wuhan 430079, China (e-mail: zxzorigin@whu.edu.cn; liuxy0319@whu.edu.cn; zhangyj@whu.edu.cn; yi.wan@whu.edu.cn; ysduan@whu.edu.cn).

Digital Object Identifier 10.1109/JSTARS.2021.3093576

The remainder of this article is organized as follows. Section II reviews the related works. Section III introduces the crucial theory for the extraction of the planar subset. Section IV describes the methodology of the proposed 3-D plane segmentation approach in detail. Section V evaluates the proposed algorithm in experimental studies. Finally, Section VI concludes the article.

II. Related Work

A. Plane Segmentation

Plane segmentation is the process of clustering points that are continuous in space into different groups, each of which forms a planar shape. The basic geometric-based plane segmentation methods can be generally divided into three categories: 1) region growing, 2) model fitting, and 3) feature clustering.

Region growing-based methods are mostly implemented with alternative and iterative processes [12]–[16]. In each iteration, one or more seed points are selected from the point cloud based on the curvature of each point; then, the neighboring points (determined by the k-nearest neighborhood algorithm mostly) of each seed point are examined to extend the growing region based on some predefined similarity criteria (e.g., normal vector and curvature). Xiao *et al.* [17] proposed a hybrid region growing (HRG) approach for organized point clouds considering two kinds of growth units: a single point or a subwindow. The region growing-based methods are usually capable of preserving the boundaries of planes, but they are very sensitive to noise because the segmentation quality relies on the selection of the seed point.

Model fitting-based methods estimate the planar parameters from the point clouds using voting techniques. Hough transform [18] and random sample consensus (RANSAC) [19] are the two most popular methods in this category. Hough transform applies accumulative voting on point clouds to extract planes, while RANSAC aims to find the planar model with the maximum number of inliers within a distance threshold. Tarsha-Kurdi *et al.* [20] combined both of these methods to 3-D building roof plane detection and claimed that RANSAC is much more efficient to detect planes, while Hough transform is very sensitive to the segmentation parameters. Numerous improved RANSAC methods for plane segmentation from 3-D point clouds have been proposed as well [21]–[24]. However, these algorithms are still limited by the quality of the input point cloud and the parameter settings. Moreover, in the case of detecting multiple planes, the inaccuracies in detecting the first plane can heavily affect the subsequent planes [5].

Feature clustering-based methods group the neighboring points based on the similarity of some geometric attributes such as the normal vector, Euclidean distance, and density. K-means clustering [25], fuzzy clustering [26], and mean-shift clustering [27] are the three commonly used clustering methods in 3-D point cloud processing. Strongly emphasizing robustness and efficiency, Kim *et al.* [28] defined the neighborhood by considering both the 3-D proximity between the points and shapes of the surfaces, and the point attributes are calculated by the defined neighboring points. Then, the dimensionally reduced attribute space is employed for the clustering process. However, the feature clustering-based methods are sensitive to noises and outliers and are commonly influenced by the neighborhood definition. To develop a robust segmentation method, complex clustering criteria can be intensively applied. However, it will greatly increase the computational cost [29].

In addition to the above three classical categories, some 2-D geometric primitive extraction methods can be extended for 3-D point clouds, such as scanline analysis [30] and global energy optimization [31]. Scanline analysis-based 3-D segmentation approaches [32], [33] segment point clouds into different scan profiles using some certain geometric constraints, such as the distances between consecutive points [32] and direction vector [33]. Thereafter, a merging operation is applied to group the scan profiles based on certain similarity criteria. Scanline analysis is fast and stable, but the segmentation results depend on the preferred orientation and its applicability is limited to structured point clouds. Energy optimization-based 3-D segmentation methods [34]–[36] utilize the basic geometric-based method aforementioned to generate the first initial plane set. Then, an energy function is constructed [37], [38] minimized by refining the points' labels. Energy optimization can effectively suppress the influence of noise and outliers in some cases, but it is restricted by the initial segmentation results and may easily fall into the local optimum. Furthermore, the computing efficiency is too low.

Recently, the utilization of 3-D voxels has become a trend in many point cloud applications to improve computational efficiency. Researchers proposed different supervoxel segmentation methods to better preserve object boundaries, such as voxel cloud connectivity segmentation [39], boundary-enhanced supervoxel segmentation [40], and toward better boundary preserved supervoxel segmentation (TBBP) [41]. Mahmoudabadi *et al.* [42] transform superpixel to supervoxel and then calculate the best-fit plane of the supervoxels by using a linear regression model. Voxel-based 3-D segmentation organizes point clouds into voxels or supervoxels and estimates their geometric features. Ultimate planes are generated by a merging process (e.g., region growing and clustering) [10], [43]–[45]. Vo *et al.* [43] use voxel as the only basic unit to generate the final plane, which greatly improves the segmentation efficiency. But the plane fitting of voxels is not imprecise when the input point cloud has a severe noise level. Dong *et al.* [10] introduced a robust and efficient 3-D plane segmentation method (REPS). They utilize a combination of multiscale planar supervoxels and individual points as the basic units and refines the initial plane set, which is generated by HRG, based on a global energy optimization framework. However, the planar supervoxels determined by the saliency features [11] still contain points on different planes and noisy. Furthermore, global energy optimization still requires large computational expense as the number of data increases. Fatemeh *et al.* [45] used the RANSAC algorithm to establish the most likely local plane from each predivided cell, which improved the geometric accuracy of the gridded-cell effectively. But it is still difficult to obtain precise local planes from the point cloud with the severe noise level.

B. A-Contrario *Theory*

In the context of *a-contrario* theory, the occurrence of any basic structures and grouping laws, so-called Gestalt, is independent in the null-hypothesis background scene, and the occurrence of a gestalt is determined to violate the Helmholtz principle if the expected value of the occurrence times, number of false alarm (NFA), is less than 1 [9]. Hence, the meaningfulness of a certain structure can be measured by estimating its NFAs. Desolneux *et al.* [46] and Desolneux *et al.* [9] initially applied this theory for image structure detection, which detects meaningful structures that cannot happen by chance under the null-hypothesis. In the field of the 2-D image, von Gioi *et al.* [47] employed *a-contrario* theory to segment lines from 2-D images and achieved convincing performance. Furthermore, *a-contrario* has been widely used in many other low-level structure detections, such as vanishing points [48], rigid sets of point matches [49], [50], histogram gaps [51], contrasted boundaries [52], junctions [53], 3-D point alignment [54], 3-D line segment [55]–[56], etc. Bughin and Almansa [57] introduced an *a-contrario* criterion, which serves as an automatic and parameter-free validation method, to detect planar patches from disparity maps. This is a very novel idea of 3-D plane detection but is only designed for disparity maps with a small number of planes.

III. Extraction of Planar Subset

A 3-D point is always considered to belong to a plane when the distance is less than a preset distance threshold. But it is difficult to balance between the accuracy and the integrity of the plane if only a hard threshold is used to determine the attribution of points. This problem can be solved in a probabilistic way based on *a-contrario* theory [57]. In this section, the planar-rigidity of a 3-D point set is treated as a gestalt that is at play and measured from the probabilistic point of view. The meaningfulness of a planar subset is defined as the expected number of subsets having the same planar-rigidity in a random distribution of the 3-D point set. Different from [57], the proposed *quasi-a-contrario* model defines a nonrigorous white noise background and the calculation of NFA is associated with the planar-rigidity of each point, which is robust to various 3-D point sets.

A. *Measuring Planar-Rigidity*

To compute the probability of the occurrence of a planar point, we define a null-hypothesis H_0 [9], which means that all the planar structures are in a random and uniform distribution. In other words, the points in the 3-D point set are assumed to be randomly distributed rather than on the same plane.

We define $\mathrm{dist}(p, \mathbb{P})$ as the Euclidean distance between the point p and the planar model $\mathbb{P}$ and a distance tolerance value τ is used to indicate that a point p can be the inlier point of $\mathbb{P}$ only when $\mathrm{dist}(p, \mathbb{P})$ is less than τ. **It is highly noted that the setting of τ is related to the precision of the input point set.** The tolerance inlier region of the given point set changes with the $\mathbb{P}$, which means that the defined situation is a nonrigorous white noise background.

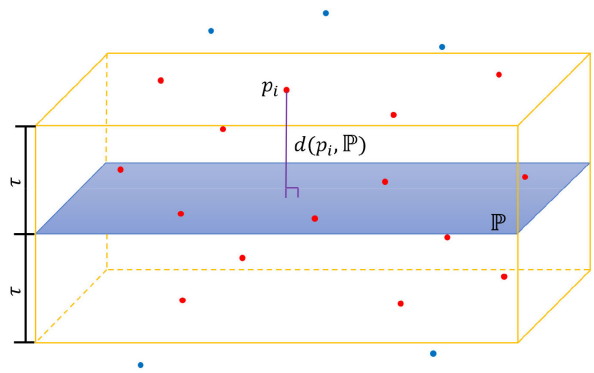

Fig. 2. Schematic representation of the planar model $\mathbb{P}$ and its tolerant inlier region. Points within the tolerant inlier region are shown in red, while others are shown in blue.

For an input point set and planar model $\mathbb{P}$, points within the tolerance inlier region are first obtained and denoted as S. Define an atom event $e_i(d)$ as the occurrence of point p_i of which the point-plane distance $\mathrm{dist}(p_i, \mathbb{P})$ is less than d, which satisfies

$$d \leq \tau. \tag{1}$$

Since p_i is randomly distributed in the tolerant inlier region under H_0, the probability of $e_i(d)$ satisfies

$$Pb\left(\mathrm{dist}\left(p_i,\ \mathbb{P}\right) \leq d | H_0\right) \leq d/\tau. \tag{2}$$

Denote the distance ratio between p_i and $\mathbb{P}$ as

$$\mathrm{DistRatio}\left(p_i,\ \mathbb{P}\right)\ =\ \mathrm{dist}\left(p_i,\ \mathbb{P}\right)/\tau. \tag{3}$$

For a particular $\mathbb{P}$ with constant distance tolerance value τ, $\mathrm{DistRatio}(p_i, \mathbb{P})$ is an incremental function of variable $\mathrm{dist}(p_i, \mathbb{P})$. As $\mathrm{DistRatio}(p_i, \mathbb{P})$ can better reflect the relationship between p_i and the tolerant inlier region, it is used to measure the geometric consistency of the points in this article. A schematic representation of $\mathbb{P}$ and its tolerant inlier region is illustrated in Fig. 2. The $\mathbb{P}$-rigidity of p_i is defined as

$$\alpha_{\mathbb{P}}\left(p_i\right)\ =\ \mathrm{DistRatio}\left(p_i,\ \mathbb{P}\right). \tag{4}$$

Set s as an arbitrary subset of S. To ensure the accuracy of measurement, the $\mathbb{P}$-rigidity of s is defined as the maximum of $\alpha_{\mathbb{P}}(p_i)$:

$$\alpha_{\mathbb{P}}\ (\mathrm{s}) = \max_{p_i \in \mathrm{s}} \alpha_{\mathbb{P}}\left(p_i\right) \tag{5}$$

which makes $\alpha_{\mathbb{P}}(\mathrm{s})$ very sensitive to non-$\mathbb{P}$ points. The global $\mathbb{P}$ rigidity of the input point set should be defined with a planar model $\mathbb{P}$ that minimizes $\alpha_{\mathbb{P}}(\mathrm{s})$.

It is quite computationally expensive to check all the potential planar models. Hence, $\mathbb{P}$ is determined by one of the possible three-subsets of the input point set, and a definition for the global planar-rigidity of 3-D points set can be given as follows:

Definition 1: A subset s with k points is α-rigid if there exists a planar model $\mathbb{P}$ associated with a subset of three points of s and satisfies

$$\alpha_{\mathbb{P}}\left(\mathrm{s}\right) \leq \alpha \tag{6}$$

where α is a positive value. Under H_0, such an α-rigid subset s satisfies

$$Pb(\alpha_{\mathbb{P}}(\mathrm{s}) \leq \alpha | H_0) \leq \alpha^{k-3}. \tag{7}$$

Proof of (7): According to the definition of $\alpha_{\mathbb{P}}(\mathrm{s})$ in (5), with a planar model $\mathbb{P}$ that is associated with a three-subset of s, $\alpha_{\mathbb{P}}(p_i) \leq \alpha$ is satisfied with every p_i in s if s is α-rigid. For the three-subset of s that is associated with $\mathbb{P}$, these three points satisfy

$$\begin{cases} \alpha_{\mathbb{P}}\ (p_i) = 0 \\ Pb\ (\alpha_{\mathbb{P}}(p_i) \leq \alpha H_0) = 1. \end{cases} \tag{8}$$

Besides, denote $\mathrm{dist}\ (p_\alpha,\ \mathbb{P}) = \alpha \cdot \tau$ as the solution of equation $\mathrm{DistRatio}\ (p_\alpha,\ \mathbb{P}) = \alpha$. Hence, the other $k-3$ points can be deduced by combining (2)–(4):

$$\begin{aligned} &Pb\ (\alpha_{\mathbb{P}}(p_i) \leq \alpha H_0) = Pb\,(\mathrm{DistRatio}\,(p_i,\ \mathbb{P}) \leq \alpha H_0) \\ &= Pb\,(\mathrm{dist}\,(p_i,\ \mathbb{P}) \leq \mathrm{dist}\,(p_\alpha,\ \mathbb{P})\, H_0) \\ &\leq \mathrm{dist}\,(p_\alpha,\ \mathbb{P})\,/\tau = \alpha. \end{aligned} \tag{9}$$

Then, by combining (8) and (9), it can be concluded that

$$Pb\ (\alpha_{\mathbb{P}}(\mathrm{s}) \leq \alpha | H_0) = \prod_{p_i \in \mathrm{s}} Pb(\alpha_{\mathbb{P}}(p_i) \leq \alpha | H_0) \leq \alpha^{k-3}. \tag{10}$$

B. Measuring the Meaningfulness of the Planar Subset

Once the planar-rigidity of a random point has been defined, the meaningfulness of the planar subset can be measured by computing its NFA; and thus, the most meaningful rigid planar subset can be obtained. Under H_0, the NFA of an α-rigid subset $\mathrm{s} \subseteq \mathrm{S}$ is defined as

$$\mathrm{NFA}(\alpha_{\mathbb{P}}(\mathrm{s}) \leq \alpha | H_0)\ = N_s\ \cdot Pb\,(\alpha_{\mathbb{P}}(\mathrm{s}) \leq \alpha H_0) \tag{11}$$

where N_s denotes the number of s of S. The smaller the $\mathrm{NFA}(\alpha_{\mathbb{P}}(\mathrm{s}) \leq \alpha | H_0)$, the more meaningful α-rigid s is (i.e., the less likely it is to appear in S under null-hypothesis H_0). We define α-rigid s is ε_0-meaningful if and only if $\mathrm{NFA}(\alpha_{\mathbb{P}}(\mathrm{s}) \leq \alpha | H_0) \leq \varepsilon_0$. Due to the complication of NFA computation, a simpler equation, which is less than or equal to $\mathrm{NFA}(\alpha_{\mathbb{P}}(\mathrm{s}) \leq \alpha | H_0)$, is also used to prove ε_0-meaningful [49]. For an α-rigid subset $\mathrm{s} \subseteq \mathrm{S}$ of k points, define

$$\varepsilon\ (\alpha, n, k) = \ (n-3) \cdot \binom{n}{k} \cdot \binom{k}{3} \cdot \alpha^{k-3}. \tag{12}$$

Proposition 1: Set S has n points, and an α-rigid subset $\mathrm{s} \subseteq \mathrm{S}$ of k points is ε_0-meaningful as soon as it satisfies $\varepsilon(\alpha, n, k) \leq \varepsilon_0$.

Proof of proposition 1: In, $(n-3)$ is the number of choices of k, $\binom{n}{k}$ is the number of subsets with k points from n points S, $\binom{k}{3}$ is the number of possible three-subsets of s used to calculate the planar model. Hence, we can easily deduce the following equation:

$$N_s \leq (n-3) \cdot \binom{n}{k} \cdot \binom{k}{3}. \tag{13}$$

Combining with (11), we have

$$\begin{aligned} &\mathrm{NFA}(\alpha_{\mathbb{P}}(\mathrm{s}) \leq \alpha | H_0)\ = N_s\ \cdot Pb\,(\alpha_{\mathbb{P}}(\mathrm{s}) \leq \alpha H_0) \\ &\leq (n-3) \cdot \binom{n}{k} \cdot \binom{k}{3} \cdot \alpha^{k-3} \\ &= \varepsilon\,(\alpha, n, k)\,. \end{aligned} \tag{14}$$

It is obvious that $\mathrm{NFA}(\alpha_{\mathbb{P}}(\mathrm{s}) \leq \alpha | H_0) \leq \varepsilon_0$ is valid if $\varepsilon(\alpha, n, k) \leq \varepsilon_0$, so Proposition 1 is proved.

C. Algorithm

According to Proposition 1, for any subset s, the meaningfulness of s can be measured by calculating $\varepsilon(\alpha, n, k)$. Hence, the most meaningful planar subset can be detected and it can be determined whether it is a meaningful plane by the smallest $\varepsilon(\alpha, n, k)$. Denote the optimal planar subset that under the planar model $\mathbb{P}$ as $\bar{\mathrm{s}}(\mathbb{P})$, which has $\bar{k}(\mathbb{P})$ points. To find such $\bar{\mathrm{s}}(\mathbb{P})$ efficiently, the points in S are sorted according to their $\mathbb{P}$-rigidities. Then, the subsets are constructed from the first k points and denoted as $\mathrm{S}(\mathbb{P}, k)$. The $\mathbb{P}$-rigidity of $\mathrm{S}(,k)$ can be denoted as $\alpha_{\mathbb{P}}(\mathrm{S}(\mathbb{P}, k))$. Since $\mathbb{P}$ is associated with the first three points, the number of points of the optimal subset and the corresponding $\bar{\mathrm{s}}(\mathbb{P})$ are defined by

$$\begin{cases} \bar{k}\ (\mathbb{P}) = \underset{k=4\to n}{\mathrm{argmin}}\ (\varepsilon\,(\alpha_{\mathbb{P}}\,(\mathrm{S}\,(\mathbb{P}, k))\,, n, k)) \\ \bar{\mathrm{s}}\ (\mathbb{P}) = \ S\left(\mathbb{P}, \bar{k}\,(\mathbb{P})\right). \end{cases} \tag{15}$$

In this article, the three-subsets associated with different $\mathbb{P}$ are randomly sampled from S. Denote $\bar{\mathrm{s}}$ as the global optimal planar subset of S, the optimal planar model $\overline{\mathbb{P}}$, the optimal number of points $\bar{k}$, and the corresponding $\bar{\mathrm{s}}$ are defined by

$$\begin{cases} \overline{\mathbb{P}} = \underset{\mathbb{P}}{\mathrm{argmin}}\ \left(\varepsilon\left(\alpha_{\mathbb{P}}\left(\mathrm{S}\left(\mathbb{P}, \bar{k}\,(\mathbb{P})\right)\right), n, \bar{k}\,(\mathbb{P})\right)\right) \\ \bar{k} = \bar{k}\ (\overline{\mathbb{P}}) \\ \bar{\mathrm{s}} = \ S\left(\overline{\mathbb{P}}, \bar{k}\right)\ . \end{cases} \tag{16}$$

Furthermore, the maximum iteration number $it_{\max}$ is adjusted according to the planar point ratio, which is denoted as $\lambda = \bar{k}/n$ [58]. $it_{\max}$ is adjusted if $\lg\bar{\varepsilon}(\mathbb{P}) < \lg\bar{\varepsilon}$ and is written as

$$it_{\max} = \begin{cases} \lg\eta / \ln\left(1-\lambda^3\right), & \text{if } \left[\lg\eta / \ln\left(1-\lambda^3\right)\right] > 10 \\ 10, & \text{if } \left[\lg\eta / \ln\left(1-\lambda^3\right)\right] \leq 10 \end{cases} \tag{17}$$

where η is the tolerance of failure, which is set as 0.01. The minimum iteration time is set as 10 to prevent exiting the loop while finding the suboptimal planar subset at the beginning of the iteration.

The pseudocode of extracting planar subset from a 3-D point set is described in Algorithm 1 as follows:

IV. Methodology of QTPS Algorithm

As discussed before, existing attempts to segment planes with voxels/supervoxels are effective but strongly limited to accurately estimate the geometric features of the voxels/supervoxels when there exists a large number of noisy points. We address this challenge by embedding *a-contrario* into a supervoxel from which we extract the planar subset as fine planar supervoxel (FPS). The proposed algorithm consists of four main steps:

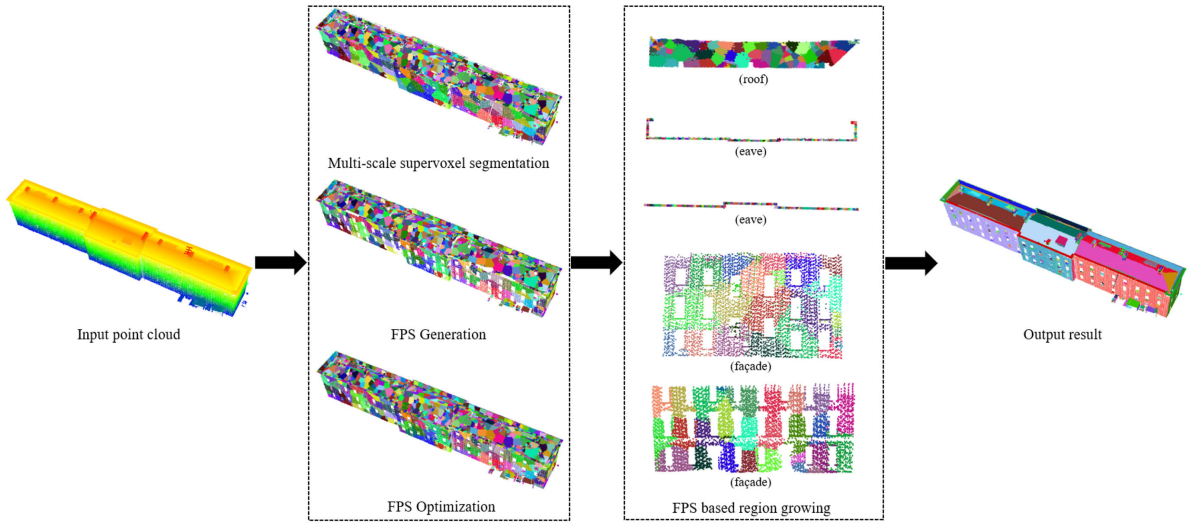

Fig. 3. Overview of the proposed 3-D plane segmentation algorithm.

Algorithm 1: Extraction of Planar Subset.

Input: point set, parameters $it_{\max}$ and τ
Output: $\bar{\mathrm{s}}$, $\mathsf{C}_{\mathbf{S}}\bar{\mathrm{s}}$, $\bar{k}$, $\lg\bar{\varepsilon}$, $\overline{\mathbb{P}}$

Initialization: $\bar{\mathrm{s}} \leftarrow \emptyset$; $\lg\bar{\varepsilon} \leftarrow \infty$; $iter \leftarrow 0$;
while $j < it_{\max}$ **do**
  sampling 3-subset to get S and $\mathbb{P}$;
  $\lg\varepsilon(\mathbb{P}) \leftarrow \infty$;
  compute the $\alpha_{\mathbb{P}}(p_i)$ of each point in S with τ;
  sort according to $\alpha_{\mathbb{P}}(p_i)$ in ascending order;
  for $k = 4 \rightarrow n$ **do**
    construct $\mathrm{S}(\mathbb{P}, k)$ with the first k points of S;
    compute NFA ($\lg\varepsilon(\alpha, n, k)$) according to (12);
    if $\lg\varepsilon(\alpha, n, k) < \lg\bar{\varepsilon}(\mathbb{P})$ **do**
$\bar{\mathrm{s}}(\mathbb{P}) \leftarrow \mathrm{S}(\mathbb{P}, k)$; $\bar{k}(\mathbb{P}) \leftarrow k$; $\lg\bar{\varepsilon}(\mathbb{P}) \leftarrow \lg\varepsilon(\alpha, n, k)$;
    end if
  end for
  if $\lg\bar{\varepsilon}(\mathbb{P}) < \lg\bar{\varepsilon}$ **do**
    $\bar{\mathrm{s}} \leftarrow \bar{\mathrm{s}}(\mathbb{P})$; $\bar{k} \leftarrow \bar{k}(\mathbb{P})$; $\lg\bar{\varepsilon} \leftarrow \lg\bar{\varepsilon}(\mathbb{P})$; $\overline{\mathbb{P}} \leftarrow \mathbb{P}$;
  end if
  $j \leftarrow j + 1$; adjust $it_{\max}$ according to (17)
end while

multiscale supervoxel segmentation, FPS generation, FPS optimization, and FPS-based region growing. Fig. 3 illustrates the overview of the proposed 3-D plane segmentation algorithm.

A. Multiscale Supervoxel Segmentation

TBBP [41] has been proven to be capable of generating better boundary-preserved supervoxels with adaptive resolution from point clouds of different densities. Supervoxel planar classification and repetitive downscaling segmentation for nonplanar supervoxels can be employed to generate coarse planar supervoxels [10]. In this article, we employ TBBP to over-segment the input points into supervoxels from maximum scale $r_{\max}$ to minimum scale $r_{\min}$, and the supervoxels are classified into planar supervoxels and nonplanar supervoxels at each scale. Downscaling supervoxel segmentation with $r \cdot r_{\Delta}$ then is continually used for the points that are classified as nonplanar supervoxels.

For each supervoxel $\mathrm{SV} = \{p_1, \ldots, p_n\}$ with n points, we calculate its covariance matrix $M_{3\times3}$, the eigenvalues $\lambda_1, \lambda_2, \lambda_3$; $(\lambda_1 \geq \lambda_2 \geq \lambda_3)$, and eigenvectors e_1, e_2, e_3 of $M_{3\times3}$ are further obtained. The saliency features g_1, g_2, g_3 [11] and curvature f_s of the supervoxel can be computed by

$$\begin{cases} g_1 = \frac{\sqrt{\lambda_1}-\sqrt{\lambda_2}}{\sqrt{\lambda_1}}, \; g_2 = \frac{\sqrt{\lambda_2}-\sqrt{\lambda_3}}{\sqrt{\lambda_1}}, \; g_3 = \frac{\sqrt{\lambda_3}}{\sqrt{\lambda_1}} \\ f_s = \frac{\lambda_3}{\lambda_1+\lambda_2+\lambda_3}. \end{cases} \tag{18}$$

Then, SV is classified by the following equation:

$$h_{\mathrm{SV}} = \begin{cases} \text{planar}, if(g_2 > g_1 \wedge g_2 > g_3 \wedge f_s < \phi) \\ \text{nonplanar}, \text{ else} \end{cases} \tag{19}$$

where ϕ is the threshold of curvature for a valid planar supervoxel. The supervoxels that are classified as nonplanar and have more than κ points will continue to implement TBBP supervoxel segmentation at a decreased scale, while supervoxels with fewer than κ points are grouped into the independent point set $\mathcal{I}$. Finally, the original input points are segmented into coarse planar supervoxel sets $\mathcal{C}$ and $\mathcal{I}$.

B. FPS Generation

Since the coarse planar supervoxels generated in the last section are planar structures, there is a high probability that a fine planar subset can be detected from each of them. In this section, each CPS in $\mathcal{C}$ is taken as the input point set to employ Algorithm 1 to get the corresponding $\bar{\mathrm{s}}$, $\mathsf{C}_{\mathbf{S}}\bar{\mathrm{s}}$, $\bar{k}$, $\lg\bar{\varepsilon}$, and $\overline{\mathbb{P}}$. The points in $\mathsf{C}_{\mathbf{S}}\bar{\mathrm{s}}$ are grouped into $\mathcal{I}$ directly. As mentioned before, the smaller the $\lg\bar{\varepsilon}$, the more meaningful the $\bar{\mathrm{s}}$ is. Hence, $\lg\bar{\varepsilon}$ can be used as a criterion to justify whether the extracted $\bar{\mathrm{s}}$ is meaningful or not. In this article, ε_t is denoted as the threshold

of $\lg\bar{\varepsilon}$, $\bar{\mathbb{s}}$ is classified as follows:

$$h_{\bar{\mathbb{s}}} = \begin{cases} FPS,\ if\ \left(\bar{k} \geq \kappa\right) \wedge \left(\lg\bar{\varepsilon} \leq \varepsilon_t\right) \\ nonplanar,\ else. \end{cases} \tag{20}$$

Those points within nonplanar $\bar{\mathbb{s}}$ are grouped into $\mathcal{I}$. The planar parameters of FPS are directly determined by the $\overline{\mathbb{P}}$. After all the CPSs have been processed, the original input points are segmented into FPS set $\mathcal{F}$ and $\mathcal{I}$. To prepare for the subsequent process, the geometric features of each FPS are calculated as follows:

$$\begin{cases} n_s\ (a_s, b_s, c_s) = e_3 \\ d_s = -\left(a_s \cdot p_s\left(x\right) + b_s \cdot p_s\left(y\right) + c_s \cdot p_s\left(z\right)\right) \\ F_s = \{p_s, n_s, d_s, f_s\} \end{cases} \tag{21}$$

where n_s is the normal vector, d_s is the parameter of the tangent plane, and F_s denotes the geometric features of the FPS.

C. FPS Optimization

$\mathcal{I}$ is composed of independent points from each of the supervoxels. However, some of the points in $\mathcal{I}$ are planar points for two reasons. First, some of the independent points from one supervoxel may belong to another FPS and therefore have not been detected as planar points. Second, the points belonging to the same planar structure are segmented into different CPSs so that the planar structure is missed. A two-step strategy is implemented to optimize $\mathcal{F}$.

In the first step, for each point that is segmented into an FPS, its adjacent points from $\mathcal{I}$ are searched by a given neighborhood search radius γ. Then group them into a candidate point set of FPS, denoted as $\{\Omega\}$. Set p_Ω as a candidate point in $\{\Omega\}$, the distance between p_Ω and FPS can be denoted as $\mathrm{dist}(p_\Omega,\ \mathrm{FPS})$. Point p_Ω will be removed from $\mathcal{I}$ to the FPS if it satisfies

$$\mathrm{dist}\left(p_\Omega,\ \mathrm{FPS}\right) \leq \delta \tag{22}$$

where δ is the threshold of $\mathrm{dist}(p_\Omega,\ \mathrm{FPS})$. For the newly added points, their adjacent points from $\mathcal{I}$ are continuously searched and regrouped until there is no newly added point for the FPS.

The next step is to find undetected planar structures by an iterative process. We take the remaining $\mathcal{I}$ as new inputs and process the previous steps repeatedly until no new FPS is generated. The points in the remaining $\mathcal{I}$ are considered as nonplanar points. Finally, the original input points are segmented into $\mathcal{F}$ and nonplanar point set $\{\mathrm{NP}\}$.

D. FPS-Based Region Growing

Region growing can effectively connect adjacent units with similar characteristics, but calculating the unit's characteristics is vulnerable to internal or external noise. FPS is considered as the basic unit for the region-growing process. The first FPS in $\mathcal{F}$ is selected as seed unit ς and removed from $\mathcal{F}$ to a plane $\mathcal{p}$. The adjacent FPSs of ς are searched by computing the 2-D concave hull of each FPS. Those adjacent FPSs with a distance less than γ are considered as the candidate growing units of $\mathcal{p}$, denoted as $\{\varpi\}$. Set ϖ as a candidate unit in $\{\varpi\}$, and denote $\varphi(\varpi, \varsigma)$, $\theta(\varpi, \varsigma)$ as the tangent plane distance and angle of normal vectors between ϖ and ς, respectively. ϖ will be removed from $\mathcal{F}$ to if it satisfies

$$\begin{cases} \varphi\left(\varpi, \varsigma\right) \leq \varphi \\ \theta\left(\varpi, \varsigma\right) \leq \theta \end{cases} \tag{23}$$

where φ and θ are the threshold of $\varphi(\varpi, \varsigma)$ and $\theta(\varpi, \varsigma)$, respectively. Those newly added FPSs are regarded as new seed units and continue to grow the $\mathcal{p}$ until no new FPS is added.

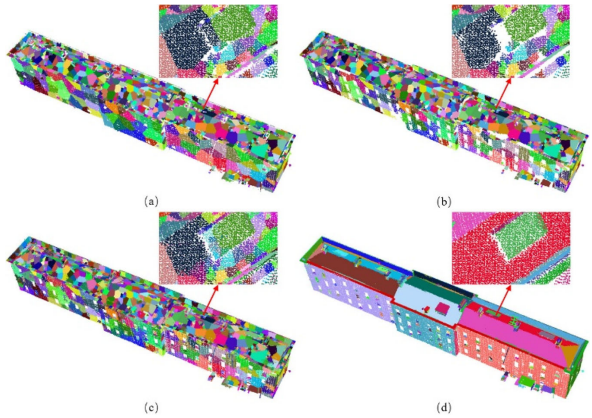

Fig. 4. Illustration of different steps' results. (a) Result of multiscale supervoxel segmentation. (b) Result of FPS Generation. (c) Result of FPS optimization. (d) Final plane segmentation result.

E. Algorithm

The pseudocode of the complete QTPS algorithm is described in Algorithm 2. To construct a robust and reliable growth unit, the input points are segmented into $\mathcal{C}$ first. Since CPS is a planar structure, the algorithm described in Section III, extraction of planar subset, is used to generate FPS from CPS according to the most meaningful planar subset's NFA, which makes FPS has very high planar accuracy. Then, $\mathcal{F}$ is optimized to ensure the integrity and recall rate of the planar structures. Finally, $\mathcal{F}$ is used as the growth unit set to obtain the final plane set. Fig. 4 shows a comparison of the results of multiscale supervoxel segmentation, FPS generation, FPS optimization, and the complete QTPS algorithm, where different supervoxels or planes are shown in different colors and key areas are shown in the small graphs.

V. Experiments

To evaluate the performance of the proposed algorithm, experiments were conducted with different types of point cloud datasets. All experiments were implemented using C++ and run on one core of an AMD RT 2950X @ 3.50 GHz CPU, with 128 GB memory.

A. Planar Subset Extraction

1) Evaluation With Simulated Data: In this section, the planar subset extraction algorithm described in Section III is evaluated with simulated data. The simulated data were created from a random planar model with 50 random 3-D points for which the plane range was controlled within 6 m∗3 m. **The distances from each planar point to the planar model were less than 0.01 m.** Then, random planar points and noise points

Algorithm 2: QTPS Plane Segmentation Algorithm.

Input: point cloud PC, parameters $it_{\max}$, $r_{\max}$, $r_{\min}$, r_{Δ}, κ, ϕ, τ, ε_t, γ, δ, φ, and θ
Output: plane set $\{\boldsymbol{p}\}$

Initialization: $\mathcal{F} \leftarrow \emptyset$; $\{\boldsymbol{p}\} \leftarrow \emptyset$;
process Multi-scale Supervoxel Segmentation with r_{max}, r_{min}, r_{Δ}, κ, ϕ to get $\mathcal{C}$ and $\mathcal{I}$;
foreach CPS in $\mathcal{C}$ **do**
  process Algorithm 1 with it_{max} and τ;
  $\mathcal{I} \leftarrow \mathcal{I} \cup \mathrm{C_S}\bar{\mathrm{s}}$
  if $(\bar{k} \geq \kappa) \wedge (\lg\bar{\varepsilon} \leq \varepsilon_t)$ **do**
    $\mathrm{FPS} \leftarrow \bar{\mathrm{s}}$; $\mathcal{F} \leftarrow \mathcal{F} \cup \mathrm{FPS}$;
  end if
  else
    $\mathcal{I} \leftarrow \mathcal{I} \cup \bar{\mathrm{s}}$;
  end else
end for
foreach FPS in $\mathcal{F}$ **do**
  Optimize FPS from $\mathcal{I}$ with γ and δ;
end for
set $\mathcal{I}$ as new input to process steps 1–15 repeatedly until no new FPS is generated;
while $\mathcal{F} \neq \emptyset$ **do**
  select the first FPS as seed point ς;
  $\boldsymbol{p} \leftarrow \varsigma$; $\mathcal{F} \leftarrow \mathcal{F} \setminus \varsigma$;
  search for $\{\varpi\}$ of ς from $\mathcal{F}$ with γ;
  foreach ϖ in $\{\varpi\}$ **do**
    if $\varphi(\varpi, \varsigma) \leq \varphi) \wedge (\theta(\varpi, \varsigma) \leq \theta)$ **do**
      $\boldsymbol{p} \leftarrow \varpi$; $\mathcal{F} \leftarrow \mathcal{F} \setminus \varpi$;
    end if
  end for
  select newly added ϖ as ς and continue to grow$\mathcal{P}$;
  $\{\boldsymbol{p}\} \leftarrow \{\boldsymbol{p}\} \cup \boldsymbol{p}$;
end while

were added and randomly distributed. **The distances from each noise point to the planar model were less than 0.3 m and larger than 0.01 m.** The number of error points was increased from 0 to 950 while keeping the total number of points to 1000. In other words, the noise point ratio, which is denoted as $\hat{p}$, increased from 0% to 95%.

To investigate the influence of the distance tolerance τ, four groups of simulation experiments were carried out by setting the τ value to 0.05, 0.1, 0.15, and 0.2 m. $it_{\max}$ was set as 500. The process of data simulation and Algorithm 1 were conducted 100 times in each group. For each group, the extracted planar subset $\bar{\mathrm{s}}$ was evaluated in terms of the following four values:

1) The average value of $\lg\bar{\varepsilon}$ from 100 times of data simulation and planar subset extraction.
2) The average recall rates. The recall rate was calculated as $N_{\overline{ps}}/N_p$, where $N_{\overline{ps}}$ denotes the number of simulated planar points in $\bar{\mathrm{s}}$ and N_p denotes the total number of simulated planar points.

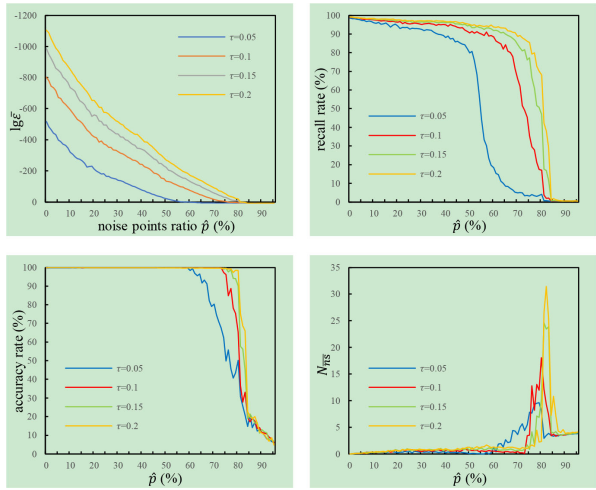

Fig. 5. Statistical curves of the groups of simulated experiments.

3) The average accuracy rates. The accuracy rate was calculated as $N_{\overline{ps}}/N_{\bar{\mathrm{s}}}$, where $N_{\bar{\mathrm{s}}}$ denotes the number of points in $\bar{\mathrm{s}}$.
4) The average number of extracted noise points $N_{\overline{ns}}$.

Fig. 5 illustrates the statistical curves of the simulation experiments, which are shown in different colors. The Helmholtz principle states that when noise with increasing variance is added, the NFA value of meaningful segment increases. And the segment is no longer detected if the NFA becomes larger than 1 [9], [47]. As can be seen in Fig. 5, the $\lg\bar{\varepsilon}$ and the number of detected noise points were increased along with the increase of $\hat{p}$, while the recall rate and accuracy rate were the opposite. When τ was set as 0.05, the recall rate and accuracy rate decreased much faster when compared to the other three settings, which means that the proposed algorithm was sensitive to the increase of $\hat{p}$ if τ was set to be too low. Moreover, although a higher setting of τ had a higher recall rate and accuracy rate with any given ratio of noise points, it was more likely to incorporate noise points into the optimal planar subset $\bar{\mathrm{s}}$, especially when $\hat{p}$ reached more than 75%. The results also show that when the value of $\lg\bar{\varepsilon}$ gradually rose to approximate 0 or even exceeded 0, the recall rate and the accuracy rate began to decrease dramatically and more noise points were detected in $\bar{\mathrm{s}}$.

In conclusion, if the required planar accuracy was less than 0.01 m, the optimal setting of τ is between 0.05 and 0.15 for improving the correctness of $\bar{\mathrm{s}}$, especially when $\hat{p}$ reached more than 75%. Additionally, the recall rate and the accuracy rate begin to decrease significantly when $\lg\bar{\varepsilon}$ reach to 0, so that 1-meaningful (i.e., $\varepsilon_0 = 1$) that introduced by Desolneux *et al.* [9] is verified to be able to justify whether a planar shape is meaningful or not. Hence, the criterion of $\lg\bar{\varepsilon} < 0$ can be used to justify the correctness of $\bar{\mathrm{s}}$, the smaller $\lg\bar{\varepsilon}$ is, the more meaningful $\bar{\mathrm{s}}$ is.

2) Evaluation With Real Data: In this section, eight representative CPSs, which were generated from dense ALS point cloud and airborne MVS point cloud by using the multiscale supervoxel segmentation, were chosen to establish the real dataset 1. These point clouds have high point density and severe noise

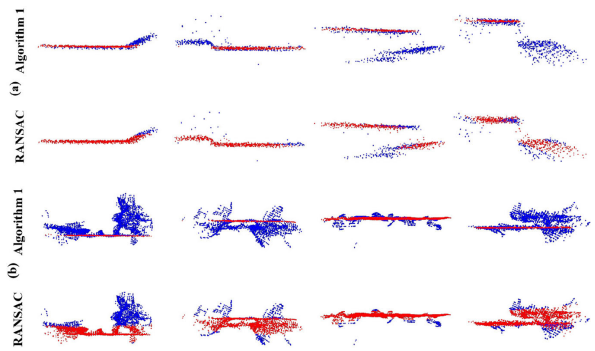

Fig. 6. Results for extracting planar subset from the 3-D point set, where the extracted planar points are shown in red and the nonplanar points are shown in blue. (a) Extraction results in dense ALS point cloud. (b) Extraction results in airborne MVS point cloud.

levels. Detailed data information will be described in Section V-B. Since RANSAC is the most effective geometric model-fitting algorithm, Algorithm 1 is compared with RANSAC to demonstrate its superiority. The value of τ and the distance threshold of RANSAC were both set as 0.1 m.

Fig. 6 illustrates the visual comparison between the results of Algorithm 1 and RANSAC, where the extracted planar points are shown in red color. The planar subsets extracted by the proposed algorithm represent well the planar structure of these diverse point sets, while the plane fitting results of RANSAC obtained incorrect planar parameters in some cases. Although RANSAC is found to be capable of improving the accuracy of extracting planar subset by reducing the distance threshold, it cannot avoid extracting incorrect planes when the noise level is very high, and the result is strongly limited by the distance threshold. The most important is that Algorithm 1 cannot only extract the correct planar subsets but also can obtain precise planar parameters even if the given point set contains many noise points.

To further evaluate the quantitative performance of the results, we derived the geometric features of each extracted planar subset and then calculated the distances between each inlier planar point to its planar model. The planar parameters are calculated according to the extraction results, so that the point distance obtained by RANSAC may be larger than the preset threshold. The quantitative statistical results are listed in Table I, including the ratio of extracted point number ($\bar{k}/n$), the maximum and mean value of the point distance. The maximum and mean values of the point distance obtained by Algorithm 1 are found to be much lower than those of the RANSAC. Although RANSAC can improve the accuracy by reducing the distance threshold, it is still constrained by the hard threshold and cannot avoid extracting incorrect models.

TABLE I
QUANTITATIVE RESULTS OF PLANAR SUBSET EXTRACTION

Data	Method	$\bar{k}/n$	Max-dist (m)	Mean-dist (m)
ALS-1	Algorithm 1	535/806	**0.046875**	**0.011375**
	RANSAC	736/806	0.101563	0.028617
ALS-2	Algorithm 1	439/749	**0.039063**	**0.013098**
	RANSAC	676/749	0.093750	0.029470
ALS-3	Algorithm 1	314/829	**0.017578**	**0.007582**
	RANSAC	574/829	0.117188	0.043949
ALS-4	Algorithm 1	227/810	**0.011719**	**0.005343**
	RANSAC	563/810	0.125000	0.045557
MVS-1	Algorithm 1	1112/3976	**0.010355**	**0.003616**
	RANSAC	2553/3976	0.137424	0.025212
MVS-2	Algorithm 1	901/3143	**0.009769**	**0.003852**
	RANSAC	2672/3143	0.133013	0.041399
MVS-3	Algorithm 1	3017/3648	**0.028990**	**0.009273**
	RANSAC	3497/3648	0.130506	0.014292
MVS-4	Algorithm 1	1047/3661	**0.008023**	**0.003096**
	RANSAC	2997/3661	0.124264	0.039523

B. 3-D Plane Segmentation

To evaluate the performance of the proposed QTPS algorithm for 3-D plane segmentation, a comparison with three state-of-the-art 3-D plane segmentation methods was conducted. The first method is the Efficient RANSAC (ER) [21], which is the most efficient and widely used method for 3-D shape detection. The second method is octree-based region growing (ORG) [43], which is proved to be effective on both terrestrial and aerial LiDAR point clouds. The third method was REPS [10], which is proved robust on both high-quality TLS point clouds and low-quality RGB-D point clouds. ER was implemented by using the public source code in CGAL.[1] ORG was implemented by using the duplicated program. The REPS results were provided by the authors.

1) Data Overview: Three different types of challenging datasets of varying noise level, density, and complexity were selected to conduct the experiments. The first dataset is dense ALS point cloud data for Dublin City Center that was obtained by Laefer *et al.* [59]. The second dataset is a sparse ALS point cloud that was captured at a rather high altitude in Ningbo, China. The third dataset is an airborne MVS point cloud that was generated from multiview images from the ISPRS benchmark of image orientations [60] by using MVE [61]. The points density, noise level, and structural complexity of the Dublin dataset are much higher than that of the Ningbo dataset due to different flight altitudes, flight paths, and LiDAR equipment. The Dortmund dataset has a much higher point density and noise level. The overview of the input point clouds and their corresponding aerial images are shown in Fig. 7.

2) Parameter Settings: For QTPS, the settings of $r_{\max}, r_{\min}$, and r_{Δ} comply with the recommendations of REPS [10]. The rest of the parameter settings and representations are listed in Table II. Among them, γ was set according to the average point distance μ. γ determines the independence and integrity of the planar structure. Increased μ means finer structures, and the distance between the points that belong to the same plane becomes smaller. Hence, the setting of γ is proportional to μ. We also consider the partial deficiency of points. γ is set as 7μ but greater than or equal to τ. τ and ε_t were set as 0.1 m and 0, respectively. Additionally, δ and φ were set as $\tau/2$ and τ, respectively, which is used to ensure the integrity and accuracy of the final planes.

[1]Online. [Available]: https://www.cgal.org/

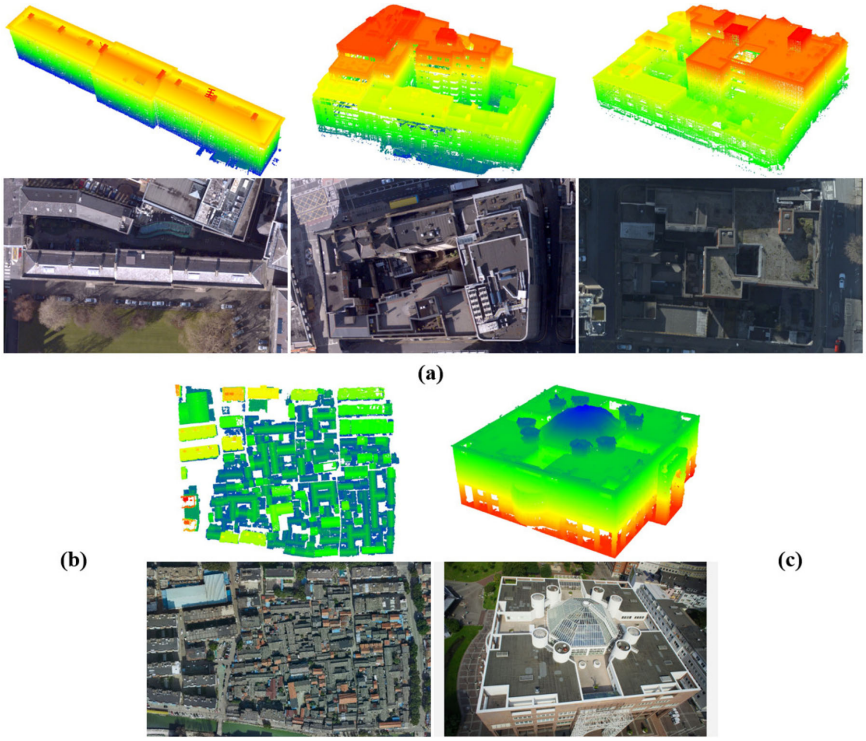

Fig. 7. Overview of the input point clouds and their corresponding aerial images. (a) Three ALS building point clouds from the Dublin dataset are denoted as D1, D2, and D3 from left to right. (b) ALS building-cluster point cloud from Ningbo dataset denoted as NB. (c) Airborne MVS point cloud of Dortmund city center, denoted as DCC.

TABLE II
PARAMETER SETTINGS AND REPRESENTATIONS

Parameter	Value	Representation
κ	20	minimum planar point number
ϕ	0.05	curvature threshold
τ	0.1m	distance tolerance value
ε_t	0	threshold of $\lg\bar{\varepsilon}$
γ	max $(7\mu, \tau)$	neighborhood search radius
δ	$\tau/2$	distance threshold between p_Ω and FPS
φ	τ	distance threshold between two planes
θ	10°	angle threshold between two planes

For ER, some of the parameters are set to refer to QTPS, including the minimum number of points of a shape (refer to κ), maximum tolerance Euclidean distance from a point and shape (refer to τ), the maximum distance between points to be considered connected (refer to γ). The probability to control search endurance and maximum tolerance normal deviation from a point's normal to the normal on a shape at the projected point is set to the default values. For ORG, r_{th} , θ_{th}, d_I, and $d_{\min}$ are set as 0.25 m, 13.0°, 1.0 m, and 0.2 m, respectively, according to the original paper.

3) Qualitative Analysis: Figs. 8 –10 illustrate the visualization comparison results of the four methods from one global view and two close-up views that are corresponding to the red rectangles in the global views. All the segmented planar points are in color according to the RGB values, where the points belonging to the same plane are shown in the same color.

More critical areas from different views can be seen in the supplementary material.

As can be seen in Fig. 8, in the Dublin dataset, the proposed QTPS segmented more precise planes, and more fine planar structures (e.g., eaves and windowsill) were preserved well. ER produced lots of under-segmentations, where some of the nonadjacent planes were merged through many noise points and some of the adjacent planes with small planar distances were merged due to the threshold problem. ORG produced lots of over-segmentations, where the geometric features of the voxel unit are strongly influenced by the noise point, which makes some of the voxels could not be merged into the corresponding planes. REPS missed a lot of planar points, especially for some planar structures with sparse points or small structures, which probably be removed in the optimization process.

The façade points of the Ningbo dataset are missing due to the situation of dense buildings and high flight altitude. In Fig. 9, both QTPS and ORG have good performance of segmenting roof planes effectively. The performance of ER and REPS was unsatisfactory. A lot of wrong planes and over-segmentations were shown in the result of the ER. REPS fails to segment sparse point clouds due to the strict optimization strategy. Furthermore, QTPS was also applied to the USGS open source point cloud,[2] which has a much lower point density, to verify its ability to process sparse point clouds. This part is shown in the supplementary material.

[2]Online. [Available]: http://www.usgs.gov/

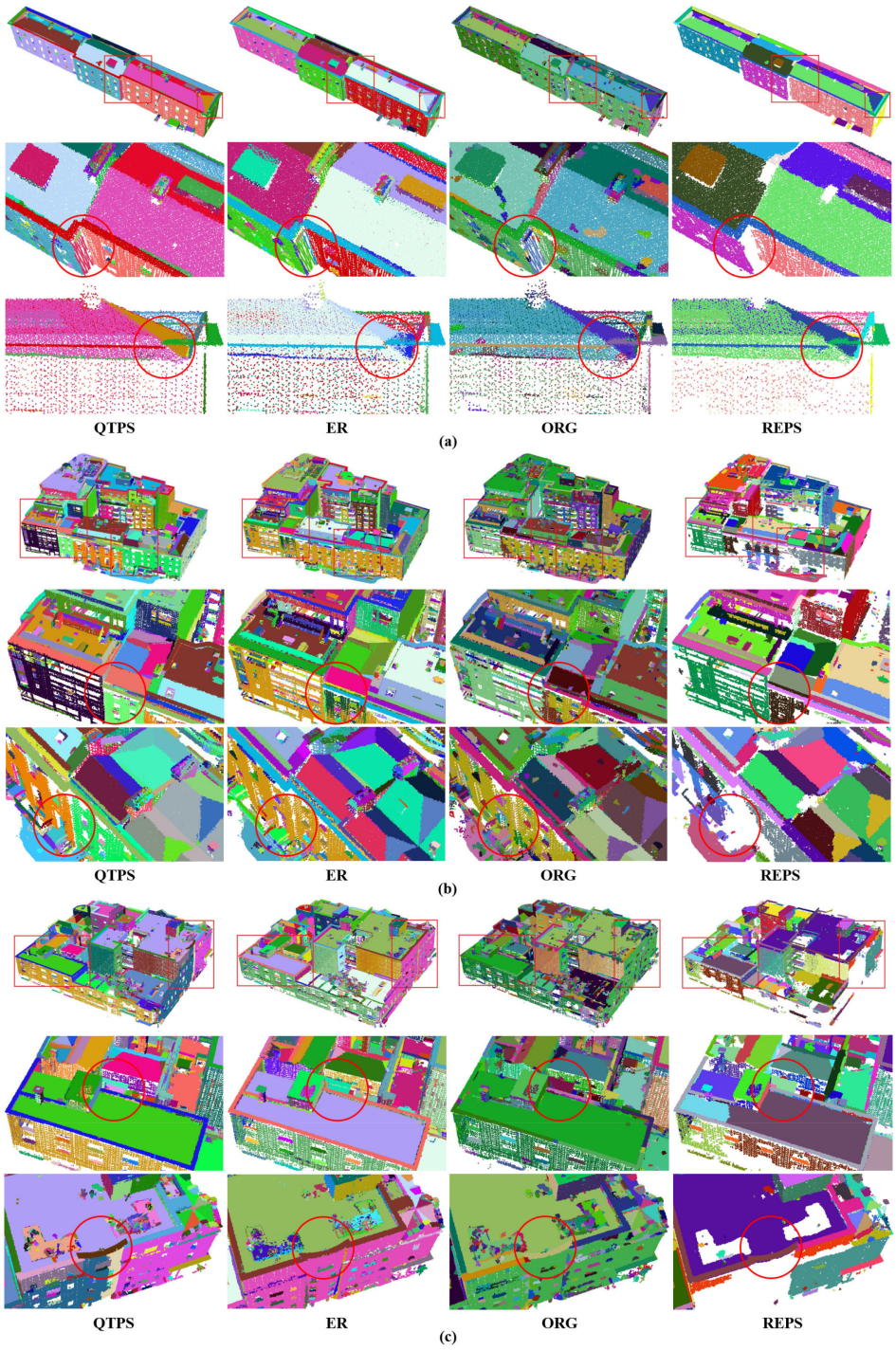

Fig. 8. Comparison of various 3-D plane segmentation results for Dublin dense ALS point clouds (front view). (a) Results of D1. (b) Results of D2. (c) Results of D3.

In Fig. 10, all four methods obtained a lot of correct planar structures from the Dortmund dataset. QTPS preserved more true positives but also segmented some pseudo planes that are constructed by noise points. ER mixed many noise points with planar points and caused the blurred boundary. ORG retained much less fine planar structures and the boundary is not accurate enough, but ORG avoided much of the pseudo planes and merged them into adjacent large planes. REPS was well adapted for dense point cloud segmentation but still limited to a large number of noise points in some complex structural parts (e.g., dome).

4) Quantitative Analysis: To evaluate the quantitative performance of the four methods, we compared the plane segmentation results of the four methods with those manually marked reference planes in terms of the following four metrics [i.e., completeness, correctness, segmentation cross-lap (SCL) rate, and reference cross-lap (RCL) rate], which are commonly used for the evaluation of segmentation result [36], [62].

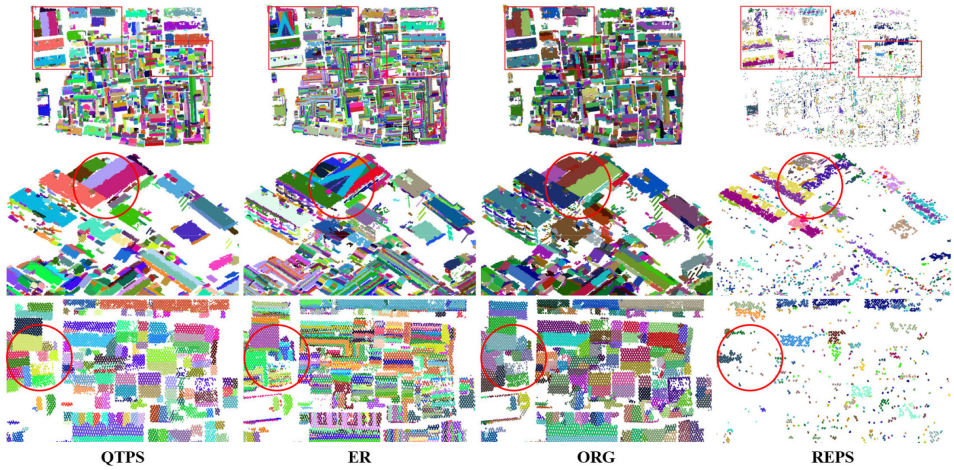

Fig. 9. Comparison of various 3-D plane segmentation results for Ningbo sparse ALS point cloud (NB).

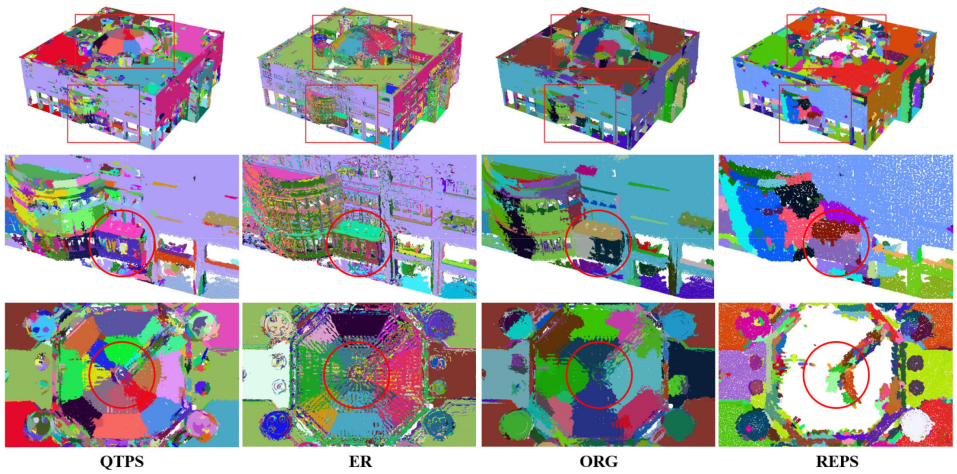

Fig. 10. Comparison of various 3-D plane segmentation results for Dortmund airborne MVS point cloud (DCC).

Completeness (comp) and correctness (corr) are defined as the number of correctly segmented planes concerning the total number of planes in the reference and segmentation results, respectively, as the following equation:

$$\begin{aligned} \text{comp} &= \frac{\text{TP}}{\text{TP}+\text{FN}} \\ \text{corr} &= \frac{\text{TP}}{\text{TP}+\text{FP}} \end{aligned} \tag{24}$$

where TP is the number of true positives (planes found both in the reference and segmentation), FN is the number of false negatives (reference planes not found in segmentation), and FP is the number of false positives (segmented planes not found in the reference). To be a true positive, a minimum overlap of 80% with the reference is required [10]. SCL rate is defined as the percentage of segmented planes that overlap multiple reference planes. RCL rate is defined as the percentage of reference planes that overlap multiple-segmented planes, as follows:

$$\begin{aligned} \text{SCL} &= \frac{N_{\text{scl}}}{N_s} \\ \text{RCL} &= \frac{N_{\text{rcl}}}{N_r} \end{aligned} \tag{25}$$

where N_{scl} is the number of segmented planes that overlap more than one reference plane, N_{rcl} is the number of reference planes that overlap more than one segmented plane, N_s and N_r are, respectively, the number of segmented planes and reference planes. Since the used datasets are too complex to label all the planes, we only marked the reference planes on the point clouds of D1 and NB for quantitative analysis, as shown in Fig. 11.

Table III lists the properties of input point clouds and their corresponding quantitative statistics. It is found that QTPS segmented the largest number of true positives in both D1 and NB point clouds.

For D1, although the building structure is not much complicated, it has a severe noise level. Fig. 12 shows a close-up view of the multiscale supervoxel segmentation result and QTPS result.

TABLE III
DATA PROPERTIES AND QUANTITATIVE STATISTICS

Data	μ (m)	#Point (M)	N_r	Method	N_s	$comp$ (%)	$corr$ (%)	RCL (%)	SCL (%)
D1	0.0561	0.3734	338	QTPS	353	91.4	87.5	4.4	7.9
				ER	472	83.7	60.0	8.3	12.3
				ORG	927	57.7	21.0	41.1	1.3
				REPS	44	8.3	63.6	11.4	20.5
NB	0.1682	0.3591	1119	QTPS	1232	83.8	76.1	6.2	1.5
				ER	2324	21.3	10.2	72.5	24.0
				ORG	1783	67.7	42.5	16.7	4.8
				REPS	80	0.2	2.5	100	0

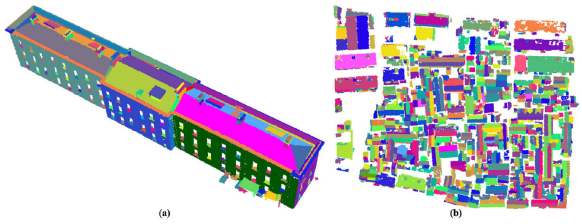

Fig. 11. Reference planes. (a) Reference planes of D1. (b) Reference planes of NB.

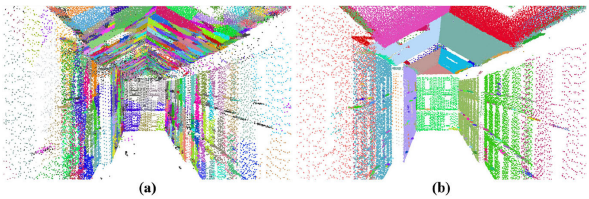

Fig. 12. Close-up view of D1. (a) Result of multiscale supervoxel segmentation, where independent points are shown in white color. (b) Result of QTPS.

A large number of noise points are distributed under the roof and around the façade [Fig. 12(a)], and they are eliminated by QTPS [Fig. 12(b)]. ER produced the largest number of SCL, which indicates that the ER is more likely to combine multiple unconnected planes for the point cloud with high density and severe noise levels. ORG produced the largest number of RCL because some of the voxel units were not merged into the corresponding planes due to the low precision of planar parameters caused by noise points. Although REPS generally avoided segmenting more incorrect planes, nevertheless it missed many reference planar structures.

For NB, the μ value reached 0.1682 m and most of the planar structures are constructed by sparse points. The performances of QTPS and ORG verified that they are robust in sparse point cloud processing. ORG can obtain voxels with higher planar precision in a low noise level point cloud.

To further evaluate the planar precision of the segmented planes, we calculated the point-plane distance from each segmented planar point to its corresponding plane, where the planar parameters of each segmented plane were calculated by (21). We calculated the maximum distance ($d_{\max}$), mean distance (d_{mean}) and RMSE of each segmented plane. Then, the average value of

TABLE IV
STATISTICS OF PLANAR PRECISION AND RUNTIMES

Data	#Point (M)	Method	$\overline{d_{max}}$ (m)	$\overline{d_{mean}}$ (m)	$\overline{RMSE}$ (m)	Runtime (s)
D1	0.3734	QTPS	**0.0863**	**0.0227**	**0.0183**	38.271
		ER	0.1447	0.0328	0.0286	**7.855**
		ORG	0.2441	0.0516	0.0446	25.205
		REPS	0.2853	0.0325	0.0323	182.317
D2	1.3206	QTPS	**0.0864**	**0.0247**	**0.0194**	239.862
		ER	0.1788	0.0445	0.0369	**112.951**
		ORG	0.2381	0.0531	0.0451	295.965
		REPS	0.2703	0.0354	0.0334	1083.275
D3	1.0842	QTPS	**0.0909**	**0.0256**	**0.0201**	167.81
		ER	0.1875	0.0466	0.0387	**59.273**
		ORG	0.2748	0.0576	0.0501	131.058
		REPS	0.2599	0.0353	0.0331	618.632
NB	0.3591	QTPS	**0.0998**	**0.0275**	**0.0208**	221.814
		ER	0.2083	0.0619	0.0458	97.010
		ORG	0.5337	0.0893	0.0869	**24.178**
		REPS	0.1625	0.0381	0.0346	275.497
DCC	2.4657	QTPS	**0.0642**	**0.0156**	**0.0225**	718.595
		ER	0.2411	0.0596	0.0478	249.954
		ORG	0.3078	0.0557	0.0470	**89.336**
		REPS	0.1372	0.0381	0.0299	3215.878

$d_{\max}$, d_{mean}, and RMSE of all segmented planes were further calculated and denoted as $\overline{d_{\max}}$, $\overline{d_{\mathrm{mean}}}$, and $\overline{\mathrm{RMSE}}$, respectively. The statistical values of $\overline{d_{\max}}$, $\overline{d_{\mathrm{mean}}}$, $\overline{\mathrm{RMSE}}$, and the runtime are listed in Table IV.

As can be seen in Table IV, QTPS provided the smallest values of $\overline{d_{\max}}$, $\overline{d_{\mathrm{mean}}}$, and $\overline{\mathrm{RMSE}}$ in each of the input data, which indicates that QTPS obtained the most precise plane fitting result.

In terms of runtime, ER had the shortest runtime in the Dublin dataset, while ORG had the shortest runtime in the Ningbo dataset and the Dortmund dataset. It should be noted that the runtime of the four methods was not only determined by the number of points, but also by the complexity of the point distribution and the number of planar structures in the point cloud.

5) Sensitive Analysis: The distance tolerance value (τ) is an essential parameter in the proposed plane segmentation approach. In Section V, we have analyzed the influence of τ on

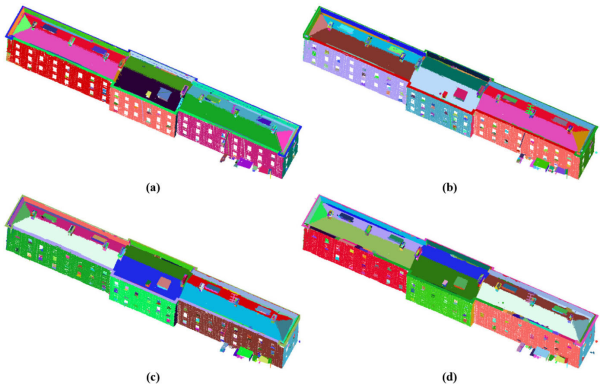

Fig. 13. Segmentation results of QTPS under different settings of τ. (a) $\tau = 0.05$ m. (b) $\tau = 0.1$ m. (c) $\tau = 0.15$ m. (d) $\tau = 0.2$ m.

the extraction of planar subset. A large τ results in low precision FPSs and further produces incorrect final planes, whereas a small one probably reduces the integrity of FPSs and miss some planar structures, which reduces the completeness of the final planes.

Different values of τ are used for the Dublin1 point cloud in Fig. 13. When τ is set to 0.05 m, the segmented planes have higher planar precision, but some fine planes are lost. When τ is set to 0.15 and 0.2 m, respectively, some of the noise points are segmented into the final planes, which make the planar precision much lower. It is seen that the eave is over segmented when τ is set to 0.2 m. In general, the results of the four-parameter settings all segmented a large proportion of true positives, which indicates that QTPS is not sensitive to the parameters when the segmentation targets are large planar structures.

6) Limitations: Although QTPS segments a large proportion of planar structures, nevertheless lots of pseudo planar structures, which are constructed by noise points and lay beyond the meaningfulness of subsequent applications, were also segmented from dense point clouds with severe noise levels. This problem can be solved by decreasing the value of τ and ε_t but at the expense of missing some of the fine planes, which makes it a difficult choice to balance. To handle the limitation mentioned above, it is better to consider more constraints (e.g., mesh topology) and make some of the parameter settings locally adaptive. Furthermore, the efficiency of QTPS is still not high enough compared to some of the existed methods.

VI. Conclusion

This article proposed a novel 3-D plane segmentation algorithm that can be applied to multiple types of point clouds. The ultimate purpose of plane segmentation is to get an accurate boundary and precise planar parameters. Based on this idea, the crucial technique of the proposed QTPS algorithm is to extract fine planar structures as basic units from presegmented coarse planar structures. A *quasi-a-contrario* theory-based algorithm is proposed to extract planar subset and a criterion is established to measure the extraction result, which can ensure the planar accuracy and prevent false-positive effectively. This result was supported by a synthetic experiment in Section V-A.

The comprehensive experimental results in Section V-B demonstrated that the proposed QTPS algorithm is robust to segment a large proportion of true positives with precise planar parameters from various airborne point clouds. The performances are favorable against state-of-the-art algorithms in the challenging problems of low point density and severe noise levels.

Our future work will focus on analyzing the topological relations between the segmented planes, thus eliminating redundant pseudo-planar structures.

Acknowledgment

The authors are grateful to the following institutions: The Urban Modelling Group at University College Dublin for providing the Dublin ALS dataset and ISPRS and EuroSDR for providing UAV images.

References

[1] Y. Zhang, X. Xiong, M. Zheng, and X. Huang, "LiDAR strip adjustment using multi-features matched with aerial images," *IEEE Trans. Geosci. Remote Sens.*, vol. 53, no. 2, pp. 976–987, Feb. 2015.

[2] S. Xu, R. Wang, and H. Zheng, "Road curb extraction from mobile LiDAR point clouds," *IEEE Trans. Geosci. Remote Sens.*, vol. 55, no. 2, pp. 996–1008, Feb. 2017.

[3] L. Nan and P. Wonka, "PolyFit: Polygonal surface reconstruction from point clouds," in *Proc. IEEE Int. Conf. Comput. Vis.*, 2017, pp. 2372–2380.

[4] Y. Verdie, F. Lafarge, and P. Alliez, "LOD generation for urban scenes," *ACM Trans. Graph.*, vol. 34, no. 3, pp. 1–14, 2015.

[5] T. Holzmann, M. Maurer, F. Fraundorfer, and H. Bischof, "Semantically aware urban 3D reconstruction with plane-based regularization," in *Proc. Eur. Conf. Comput. Vis.*, 2018, pp. 487–503.

[6] A. Sampath and J. Shan, "Segmentation and reconstruction of polyhedral building roofs from aerial lidar point clouds," *IEEE Trans. Geosci. Remote Sens.*, vol. 48, no. 3, pp. 1554–1567, Mar. 2010.

[7] T. T. Pham, M. Eich, I. Reid, and G. Wyeth, "Geometrically consistent plane extraction for dense indoor 3D maps segmentation," in *Proc. IEEE/RSJ Int. Conf. Intell. Robots Syst.*, 2016, pp. 4199–4204.

[8] S. Chen, L. Nan, R. Xia, J. Zhao, and P. Wonka, "PLADE: A plane-based descriptor for point cloud registration with small overlap," *IEEE Trans. Geosci. Remote Sens.*, vol. 58, no. 4, pp. 2530–2540, Apr. 2020.

[9] A. Desolneux, L. Moisan, and J. M. Morel, *From Gestalt Theory to Image Analysis: A Probabilistic Approach*. Berlin, Germany: Springer Science & Business Media, 2007.

[10] Z. Dong, B. Yang, P. Hu, and S. Scherer, "An efficient global energy optimization approach for robust 3D plane segmentation of point clouds," *ISPRS J. Photogramm. Remote Sens.*, vol. 137, pp. 112–133, 2018.

[11] B. Yang, Z. Dong, G. Zhao, and W. Dai, "Hierarchical extraction of urban objects from mobile laser scanning data," *ISPRS J. Photogramm. Remote Sens.*, vol. 99, pp. 45–57, 2015.

[12] P. J. Besl and R. C. Jain, "Segmentation through variable-order surface fitting," *IEEE Trans. Pattern Anal. Mach. Intell.*, vol. 10, no. 2, pp. 167–192, Mar. 1988.

[13] H. Wu, X. Zhang, W. Shi, S. Song, A. Cardenas-Tristan, and K. Li, "An accurate and robust region-growing algorithm for plane segmentation of TLS point clouds using a multiscale tensor voting method," *IEEE J. Sel. Topics Appl. Earth Observ. Remote Sens.*, vol. 12, no. 10, pp. 4160–4168, Oct. 2019.

[14] T. Rabbani, F. A. Van Den Heuvel, and G. Vosselmann, "Segmentation of point clouds using smoothness constraint," *ISPRS J. Photogramm. Remote Sens.*, vol. 36, no. 5, pp. 248–253, 2006.

[15] A. Nurunnabi, D. Belton, and G. West, "Robust segmentation in laser scanning 3D point cloud data," in *Proc. Int. Conf. Digit. Image Comput. Techn. Appl.*, 2012, pp. 1–8.

[16] E. El-Sayed, R. F. Abdel-Kader, H. Nashaat, and M. Marei, "Plane detection in 3D point cloud using octree-balanced density down-sampling and iterative adaptive plane extraction," *IET Image Proc.*, vol. 12, no. 9, pp. 1595–1605, 2018.

[17] J. Xiao, J. Zhang, B. Adler, H. Zhang, and J. Zhang, "Three-dimensional point cloud plane segmentation in both structured and unstructured environments," *Robot. Auton. Syst.*, vol. 61, no. 12, pp. 1641–1652, 2013.

[18] P. V. C. Hough, "Method and means for recognizing complex patterns," Google Patents 3069654, Dec. 18 1962.
[19] M. A. Fischler and R. C. Bolles, "Random sample consensus: A paradigm for model fitting with applications to image analysis and automated cartography," *Commun. ACM*, vol. 24, no. 6, pp. 381–395, 1981.
[20] T.-F. Kurdi, T. Landes, and P. Grussenmeyer, "Hough-transform and extended RANSAC algorithms for automatic detection of 3D building roof planes from lidar data," in *Proc. ISPRS Workshop Laser Scanning SilviLaser*, 2007, pp. 407–412.
[21] R. Schnabel, R. Wahl, and R. Klein, "Efficient RANSAC for point cloud shape detection," *Comput. Graph. Forum*, vol. 26, no. 2, pp. 214–226, 2007.
[22] T. M. Awwad, Q. Zhu, Z. Du, and Y. Zhang, "An improved segmentation approach for planar surfaces from unstructured 3D point clouds," *Photogramm. Rec.*, vol. 25, pp. 5–23, 2010.
[23] D. Chen, L. Zhang, P. T. Mathiopoulos, and X. Huang, "A methodology for automated segmentation and reconstruction of urban 3-D buildings from ALS point cloud," *IEEE J. Sel. Topics Appl. Earth Observ. Remote Sens.*, vol. 7, no. 10, pp. 4199–4217, Oct. 2014.
[24] L. Li, F. Yang, H. Zhu, D. Li, Y. Li, and L. Tang, "An improved RANSAC for 3D point cloud plane segmentation based on normal distribution transformation cells," *Remote Sens.*, vol. 9, no. 5, 2017, Art. no. 433.
[25] A. Sampath and J. Shan, "Clustering based planar roof extraction from lidar data," in *Proc. Amer. Soc. Photogramm. Remote Sens. Annu. Conf.*, 2006, pp. 5–6.
[26] J. M. Biosca and J. L. Lerma, "Unsupervised robust planar segmentation of terrestrial laser scanner point clouds based on fuzzy clustering methods," *ISPRS J. Photogramm. Remote Sens.*, vol. 63, pp. 84–98, 2008.
[27] W. Yao, S. Hinz, and U. Stilla, "Object extraction based on 3D-segmentation of lidar data by combining mean shift with normalized cuts: Two examples from urban areas," in *Proc. Joint Urban Remote Sens. Event*, 2009, pp. 20–22.
[28] C. Kim, A. Habib, M. Pyeon, G. Kwon, J. Jung, and J. Heo, "Segmentation of planar surfaces from laser scanning data using the magnitude of normal position vector for adaptive neighborhoods," *Sensors*, vol. 16, no. 2, 2016, Art. no. 140.
[29] Y. Xu, W. Yao, L. Hoegner, and U. Stilla, "Unsupervised segmentation of point clouds from buildings using hierarchical clustering based on gestalt principles," *IEEE J. Sel. Topics Appl. Earth Observ. Remote Sens.*, vol. 11, no. 11, pp. 4270–4286, Nov. 2018.
[30] A. Hoover *et al.*, "An experimental comparison of range image segmentation algorithms," *IEEE Trans. Pattern Anal. Mach. Intell.*, vol. 18, no. 7, pp. 673–689, Jul. 1996.
[31] A. Vitti, "The Mumford-Shah variational model for image segmentation: An overview of the theory, implementation and use," *ISPRS J. Photogramm. Remote Sens.*, vol. 69, pp. 50–64, 2012.
[32] C. Cabo, S. G. Cortés, and C. Ordoñez, "Mobile laser scanner data for automatic surface detection based on line arrangement," *Automat. Construction*, vol. 58, pp. 28–37, 2015.
[33] H. Nguyen, D. Belton, and P. Helmholz, "Planar surface detection for sparse and heterogeneous mobile laser scanning point clouds," *ISPRS J. Photogramm. Remote Sens.*, vol. 151, pp. 141–161, 2019.
[34] T. T. Pham, T. Chin, J. Yu, and D. Suter, "The random cluster model for robust geometric fitting," *IEEE Trans. Pattern Anal. Mach. Intell.*, vol. 36, no. 8, pp. 1658–1671, Aug. 2014.
[35] L. Wang, C. Shen, F. Duan, and P. Guo, "Energy-based multi-plane detection from 3D point clouds," in *Proc. Int. Conf. Neural Inf. Process.*, 2016, pp. 715–722.
[36] J. Yan, J. Shan, and W. Jiang, "A global optimization approach to roof segmentation from airborne lidar point clouds," *ISPRS J. Photogramm. Remote Sens.*, vol. 94, pp. 183–193, 2014.
[37] A. Delong, A. Osokin, H. N. Isack, and Y. Boykov, "Fast approximate energy minimization with label costs," *Int. J. Comput. Vis.*, vol. 1, no. 96, pp. 1–27, 2012.
[38] H. Isack and Y. Boykov, "Energy-based geometric multi-model fitting," *Int. J. Comput. Vis.*, vol. 97, no. 2, pp. 123–147, 2012.
[39] J. Papon, A. Abramov, M. Schoeler, and F. Worgotter, "Voxel cloud connectivity segmentation—Supervoxels for point clouds," in *Proc. IEEE Conf. Comput. Vis. Pattern Recognit.*, 2013, pp. 2027–2034.
[40] S. Song, H. Lee, and S. Jo, "Boundary-enhanced supervoxel segmentation for sparse outdoor lidar data," *Electron. Lett.*, vol. 50, no. 25, pp. 1917–1919, 2014.
[41] Y. Lin, C. Wang, D. Zhai, W. Li, and J. Li, "Toward better boundary preserved supervoxel segmentation for 3D point clouds," *ISPRS J. Photogramm. Remote Sens.*, vol. 143, pp. 39–47, 2018.
[42] H. Mahmoundabadi, T. Shoaf, and M. J. Olsen, "Superpixel clustering and planar fit segmentation of 3D LIDAR point clouds," in *Proc. Int. Conf. Comput. Geospatial Res. Appl.*, 2013, pp. 1–7.
[43] A. V. Vo, L. Truong-Hong, and D. F. Laefer, "Octree-based region growing for point cloud segmentation," *ISPRS J. Photogramm. Remote Sens.*, vol. 104, pp. 88–100, 2015.
[44] Y. Xu, S. Tuttas, and U. Stilla, "Segmentation of 3D outdoor scenes using hierarchical clustering structure and perceptual grouping laws," in *Proc. 9th IAPR Workshop Pattern Recognit. Remote Sens.*, 2016, pp. 1–6.
[45] F. Hamid-Lakzaeian, "Structural-based point cloud segmentation of highly ornate building façades for computational modeling," *Automat. Construction*, vol. 108, 2019, Art. no. 102892.
[46] A. Desolneux, L. Moisan, and J.-M. Morel, "Meaningful alignments," *Int. J. Comput. Vis.*, vol. 40, pp. 7–23, 2000.
[47] R. G. von Gioi, J. Jakubowicz, J.-M. Morel, and G. Randall, "LSD: A fast line segment detector with a false detection control," *IEEE Trans. Pattern Anal. Mach. Intell.*, vol. 32, no. 4, pp. 722–732, Apr. 2010.
[48] A. Almansa, A. Desolneux, and S. Vamech, "Vanishing point detection without any *a priori* information," *IEEE Trans. Pattern Anal. Mach. Intell.*, vol. 25, no. 4, pp. 502–507, Apr. 2003.
[49] L. Moisan, P. Moulon, and P. Monasse, "Automatic homographic registration of a pair of images, with a contrario elimination of outliers," *Image Process. Line*, vol. 2, pp. 56–73, 2012.
[50] Y. Wan, Y. Zhang, and X. Liu, "An a-contrario method of mismatch detection for two-view pushbroom satellite images," *ISPRS J. Photogramm. Remote Sens.*, vol. 153, pp. 123–136, 2019.
[51] J. Delon, A. Desolneux, J. Lisani, and A. Petro, "Histogram analysis and its applications to fast camera stabilization," in *Proc. Int. Workshop Syst., Signals Image Process., Ambient Multimedia*, 2004, pp. 431–434.
[52] F. Cao, P. Musé, and F. Sur, "Extracting meaningful curves from images," *J. Math. Imag. Vis.*, vol. 22, pp. 159–181, 2005.
[53] N. Xue, G. Xia, X. Bai, L. Zhang, and W. Shen, "Anisotropic-scale junction detection and matching for indoor images," *IEEE Trans. Image Process.*, vol. 27, no. 1, pp. 78–91, Jan. 2018.
[54] A. Gomez, G. Randall, and R. G. von Gioi, "A contrario 3D point alignment detection algorithm," *Image Process. Line*, vol. 7, pp. 399–417, 2017.
[55] Y. Lin *et al.*, "Line segment extraction for large scale unorganized point clouds," *ISPRS J. Photogramm. Remote Sens.*, vol. 102, pp. 172–183, 2015.
[56] Y. Lin, C. Wang, B. Chen, D. Zai, and J. Li "Facet segmentation-based line segment extraction for large-scale point clouds," *IEEE Trans. Geosci. Remote Sens*, vol. 55, no. 9, pp. 4839–4854, Sep. 2017.
[57] E. Bughin and A. Almansa, "Planar patch detection for disparity maps," in *Proc. 3DPVT*, 2010, pp. 1–8.
[58] Y. Wan and Y. Zhang, "The P2L method of mismatch detection for push broom high-resolution satellite images," *ISPRS J. Photogramm. Remote Sens.*, vol. 130, pp. 317–328, 2017.
[59] D. F. Laefer, S. Abuwarda, A. V. Vo, T.-L. Hong, and H. Gharibi, *2015 Aerial Laser and Photogrammetry Survey of Dublin City Collection Record*. 2015, [Online]. Available: https://geo.nyu.edu/catalog/nyu-2451-38684
[60] F. Nex, M. Gerke, F. Remondino, H.-J. Przybilla, M. Bäumker, and A. Zurhorst, "ISPRS benchmark for multi-platform photogrammetry," in *Proc. ISPRS Ann. Photogramm., Remote Sens. Spatial Inf. Sci.*, 2015, pp. 135–142.
[61] S. Fuhrmann, F. Langguth, and M. Goesele, "MVE-A multi-view reconstruction environment," in *Proc. Eurograph. Workshop Graph. Cultural Heritage*, 2014, pp. 11–18.
[62] M. Awrangjeb, M. Ravanbakhsh, and C. S. Fraser, "Automatic detection of residential buildings using LIDAR data and multispectral imagery," *ISPRS J. Photogramm. Remote Sens.*, vol. 65, no. 5, pp. 457–467, 2010.

Xianzhang Zhu received the B.S. degree in geographic information system from the China University of Geosciences, Wuhan, China, in 2015. He is currently working toward the Ph.D. degree in Photogrammetry and remote sensing at the School of Remote Sensing and Information Engineering, Wuhan University, Wuhan, China.

His research interests include image registration, point cloud processing, 3-D reconstruction, and mesh processing.

Xinyi Liu received the B.S. and Ph.D. degrees in photogrammetry and remote sensing from the School of Remote Sensing and Information Engineering, Wuhan University, Wuhan, China, in 2014 and 2020, respectively.

She is currently a Postdoctor with Wuhan University. Her research interests include 3-D reconstruction, LiDAR and image integration, and texture mapping.

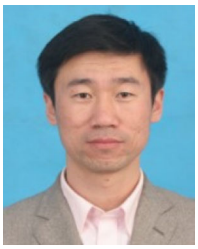

Yongjun Zhang received the B.S. degree in geodesy, the M.S. degree in geodesy and surveying engineering, and the Ph.D. degree in geodesy and photography from Wuhan University, Wuhan, China, in 1997, 2000, and 2002, respectively.

He is currently a Dean with the School of Remote Sensing and Information Engineering, Wuhan University, Wuhan, China. Since 2006, he has been a Full Professor with the School of Remote Sensing and Information Engineering, Wuhan University. From 2014 to 2015, he was a Senior Visiting Fellow with the Department of Geomatics Engineering, University of Calgary, Calgary, AB, Canada. From 2015 to 2018, he was a Senior Scientist with Environmental Systems Research Institute, USA. He has authored/coauthored more than 150 research articles and 1 book. He holds 25 Chinese patents and 26 copyright registered computer software. His research interests include aerospace and low-attitude photogrammetry, image matching, combined block adjustment with multisource datasets, object information extraction and modeling with artificial intelligence, integration of LiDAR point clouds and images, and 3-D city model reconstruction.

Yi Wan received the B.S. and Ph.D. degrees in photogrammetry and remote sensing from the School of Remote Sensing and Information Engineering, Wuhan University, Wuhan, China, in 2013 and 2018, respectively.

He is currently a Postdoctor with Wuhan University. His research interests include space, aerial, and low altitude photogrammetry, image matching, and geometric correction of multisource remote sensing data.

Yansong Duan received the M.S. and Ph.D. degrees in photogrammetry and remote sensing from Wuhan University, Wuhan, China, in 2009 and 2016, respectively.

He is currently an Associate Professor with the School of Remote Sensing and Information Engineering, Wuhan University. His research interests include photogrammetry, image matching, 3-D city reconstruction, and high-performance computing with GPU.